Mobil Solar Energy Corporation
16 Hickory Drive
Waltham, Massachusetts 02254

STRESS STUDIES IN EFG

Program Manager: Juris P. Kalejs

Quarterly Progress Report - Subcontract No. 956312

Covering Period: July 1, 1983 to September 30, 1983

Distribution Date: December 15, 1983

Mobil Solar Energy Corporation
16 Hickory Drive
Waltham, Massachusetts 02254

STRESS STUDIES IN EFG

Program Manager: Juris P. Kalejs

Quarterly Progress Report - Subcontract No. 956312

Covering Period: July 1, 1983 to September 30, 1983

Distribution Date: December 15, 1983

ABSTRACT

Experimental work in support of stress studies in high speed silicon sheet growth has been emphasized in this quarter. Creep experiments utilizing four-point bending have been made in the temperature range from $1000^{\circ}C$ to $1360^{\circ}C$ in CZ silicon as well as on EFG ribbon. Creep is found to be strong, even at the lower temperatures. Important differences in primary creep are observed with silicon impurity content in the higher temperature regions.

A method to measure residual stress over large areas using laser interferometry to map strain distributions under load is under development. The experimental system to make these measurements on CZ silicon has been built and tested.

A fiber optics sensor to measure ribbon temperature profiles has been constructed and is being tested in a ribbon growth furnace environment. It has been necessary to enclose the optical fibers in a water-cooled jacket to improve reproducibility and reliability of the sensor.

Stress and temperature field modeling work has been directed toward improving various aspects of the finite element computing schemes. Difficulties in computing stress distributions with a very high creep intensity and with non-zero interface stress have been encountered and additional development of the numerical schemes to cope with these problems is required. Temperature field modeling has been extended to include the study of heat transfer effects in the die and meniscus regions and efforts are underway to improve the overall scheme of calculating interface region temperature profiles for real system geometries.

Preceding Page Blank

TABLE OF CONTENTS

List of Figures

List of Tables

Preceding Page Blank

I. INTRODUCTION

A satisfactory model that can account for stresses generated in silicon sheet grown at high speeds is not yet available. Many attempts to calculate residual stresses have been made, but all of these suffer from inadequacies in one area or another. This report describes the work in progress under this subcontract to attempt to develop and test in the laboratory a stress-temperature field model for silicon ribbon EFG. In one subtask, a computer code developed at Harvard University to calculate stress with plastic deformation in steady-state sheet growth is being applied to study temperature field-stress relationships. The stress state is parameterized by a two-dimensional temperature field and growth speed. Incorporation of time dependent stress relaxation effects is through a creep law to model the impact of plastic flow on the sheet residual stress state. A second aspect of the program deals with the development of a model to predict the temperature field in a moving sheet from given system component temperatures (i.e., the sheet environment), and studies experimental means to verify the model. This work is attempting to integrate temperature field modeling in the solid which takes into account real system geometries with a more detailed heat transfer model developed at MIT for the die top and meniscus regions below the growth interface.

The predictions of the stress analysis and temperature field models are supported on a qualitative level by experimental results obtained from characterization of 10 cm wide ribbon grown in an EFG cartridge system. Residual stresses in both buckled and unbuckled as-grown ribbon are much lower than predicted for the thermoelastic case. These can only be achieved through high rates of creep for the temperature profiles that are calculated for the 10 cm ribbon. Defects are observed in the ribbon cross section which originate from stress instabilities.

Both modeling and experimental work are in progress to attempt to apply the stress analysis at a more quantitative level. The modeling is examining stress-temperature field relationships in a search for low stress growth configurations. The experimental efforts are in study of the high temperature creep response of silicon to provide information on the constitutive relationship, development of a technique to measure the temperature field in the sheet during growth, and of means to measure residual stress distributions. A temperature sensor based on fiber optics has been constructed for the temperature field measurements. A laser interferometry technique is being evaluated for residual stress measurements at the University of Illinois.

Attempts to verify aspects of the stress and temperature field modeling with the 10 cm cartridge system have met with limited success. Due to the complexity of the growth interface environment it has not been possible to use the fiber optics sensor. The cartridge system has lacked flexibility to allow imposition of changes in growth conditions and system temperature fields in a known and controllable manner in order to study temperature field-stress relationships at a quantitative level. A system that has the required flexibility for testing of the stress analysis model is being constructed.

II. PROGRESS REPORT

The work carried out on development of understanding of stress generating mechanisms in vertical silicon sheet growth is described in the next four sections.
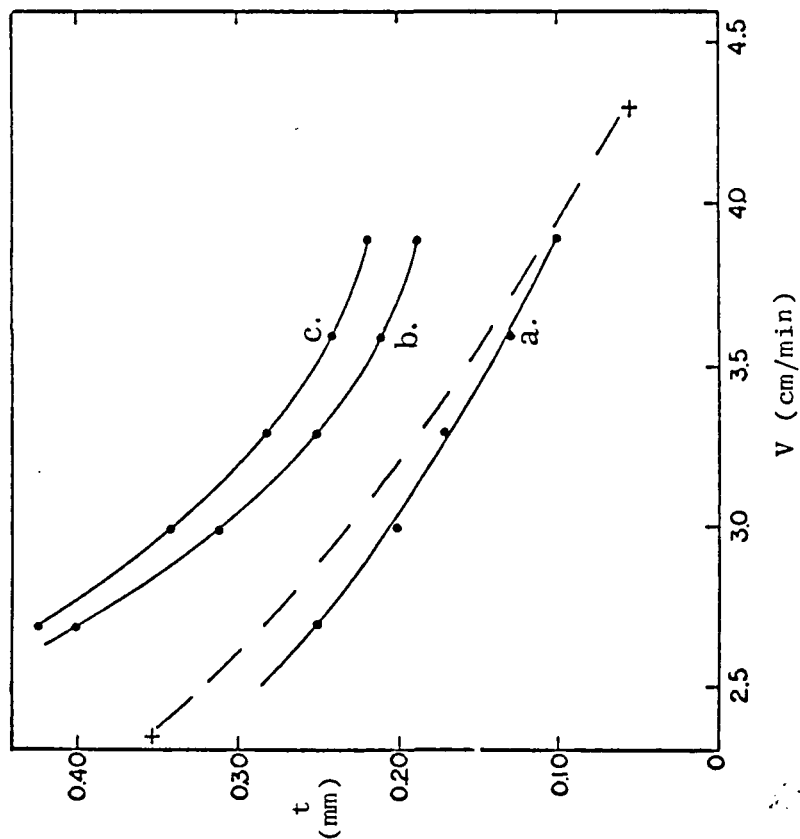
A. Advanced System Design

1. Temperature Field Modeling (H.M. Ettouney and R.A. Brown, MIT)

The finite element analysis techniques developed for solution of coupled capillary and heat and mass transfer equations in the EFG system have been applied to study the 10 cm cartridge system [1]. Experimental data have been obtained for known environment temperature configurations of the ribbon on the thickness-velocity relationship and on aluminum segregation through the ribbon thickness. The latter gives information on the interface shape. The data will be used to test certain aspects of the heat transfer model in use and thus to obtain information on the dominant heat transfer parameters influencing ribbon temperature distributions. This information will be used in stress analysis to help in placing these calculations on a more quantitative level.

In the following, we report the fitting results of the theoretical predictions by the finite element model developed in [1] and the experimentally measured field variables. In the first part, variations in the crystal thickness as a function of growth rate are fitted by solution of the thermal/capillary problem, which includes simultaneous solution of the energy balance equations in melt, solid, and die and the Young-Laplace stress balance equation. In the second part, dopant segregation along the melt/solid interface is compared to the experimental measurements. The theoretical results are obtained by solving the momentum and the mass transfer equations using the technique presented in [2].

a. Fitting of the Crystal Thickness - Velocity Data

Figure 1a shows the measured variations in the crystal thickness as the growth rate is increased from 2.5 to 4 cm/minute. Figure 1b shows the axial temperature profile of the surroundings during the experiment. Crystal thickness measured at the right, center and left sides of the sheets is shown as curves a, b, and c in Fig. 1a, respectively. The left and right measurements are made at a distance of 1 cm from the edges of the crystal. The changes in the crystal thickness along the same horizontal level are caused by nonuniformities in the rate of heating in the die. The surrounding temperature profile shown in Figure 1b is driven by a water cooler and afterheater. The cooler is placed at a distance of 0.2 cm from the top of the die and has a length of 0.3 cm. The afterheater has a constant temperature gradient of 50°K/cm and its high temperature setting is equal to 1473°K. At both ends of the cooler there are rapid increases in the surrounding temperature followed by a linear increase to the heater temperature, downstream of the cooler, and by a linear increase to a temperature close to the die temperature upstream of the cooler. The dimensionless temperatures of the surroundings are shown on Figure 1b.

Fig. 1b. Experimental (environment) vertical temperature profile in 10 cm EFG cartridge and calculated ribbon distribution.

(b)

(a)

Fig. 1a. Thickness-velocity curves for 10 cm cartridge system with cold shoes at a face heater temperature setting of 1431°C. The dashed line is for a continuously imposed velocity change that terminated in a ribbon pull-out or meniscus break at the highest speed.

4

The finite element model described in detail in reference [1] is used to fit curve a in Figure 1a. In this model the values of the thermophysical properties used to characterize molten and solid silicon and the die material are the same as those given in Table II of reference [1], except for the thermal conductivity of solid silicon which is taken to be temperature independent there. Here, it is redefined according to the relation $K(x,y) = (K_M/T_M)/T(x,y)$, where K_M is the solid phase thermal conductivity at the melting point, 0.22 J/s°K/cm. The height and length of the die base and tip are the same as those given in reference [1], Table I. The capillary spacing and the static head are taken equal to be 0.05 cm and 4 cm, respectively, and the surrounding temperature profile given in Figure 1b is used. These specifications define all the system parameters except for the die base temperature, $\tilde{T}_o$, and the surrounding temperature at the die base, $\tilde{T}_\infty^o$. The two unspecified parameters are carefully varied within a realistic range; i.e., $T_M + 20 < \tilde{T}_o < T_M + 50°K$ and $\tilde{T}_\infty^o \simeq \tilde{T}_o$, in order to obtain the best theoretical fit to the experimental measurements. The resulting fit is shown in Figure 2 and the calculated axial temperature profile along the surface at a growth rate of 4 cm/minute is shown together with the surrounding temperature profile in Figure 1b. The best fit was obtained for $\tilde{T}_o =$ 1727°K and $\tilde{T}_\infty^o = 1733°K$. The sensitivity of these results with respect to variations in the two fitting parameters was examined. It is found that to achieve a 50% increase in the crystal thickness, the die temperature needed to be decreased by 13°K (compare the two curves in Figure 2 for $\tilde{T}_o = 1727°K$ and $\tilde{T}_o =$ 1714°K). On the other hand, large adjustments in $\tilde{T}_\infty^o$, at a constant $\tilde{T}_o$, were required to achieve the same degree of change in the crystal thickness. For example, the crystal thickness was increased from 0.008 to 0.013 cm, at a growth rate of 4 cm/minute and a die temperature of 1727°K, when $\tilde{T}_\infty^o$ was decreased from 1961°K to 1372°K.

b. Fitting of Dopant Segregation

Calculations of the dopant distribution in the melt and its segregation along the melt/solid interface are more complicated than the heat transfer calculations since they require calculations of the flow field. The mass and momentum equations and the finite element approximation for the field variables are given in detail in [2]. The fit for the dopant segregation is compared with the experimentally measured aluminum profiles shown in Figure 3. The three profiles are measured along the crystal thickness at right, center and left, Figures 3a, 3b and 3d, of the crystal at a growth rate of 2.6 cm/minute for the same samples as in Figure 1a. In these three profiles the average aluminum segregation and operating conditions of the solid curve in Figure 2, defined as the ratio between the difference of the solute concentration at the surface and the centerline to the bulk concentration, varies between 10 and 20%, excluding that caused by a structural defect (e.g., a grain boundary) in the center of Figure 3c.

To analyze the theoretical predictions of the solute profiles, one has to take into account shapes of the melt/solid interface and the flow field pattern. In Figure 4a, the displayed melt/solid interfaces are concave, as viewed from the melt, and their deflections, defined as the ratio between the difference of the interface height at the centerline and the surface to the crystal thickness, are 1.1, 1, 0.9. and 0.78 at growth rates of 2.5, 3, 3.5, and 4 cm/minute. As discussed in references [2] and [3], such interface shape always results in a

5
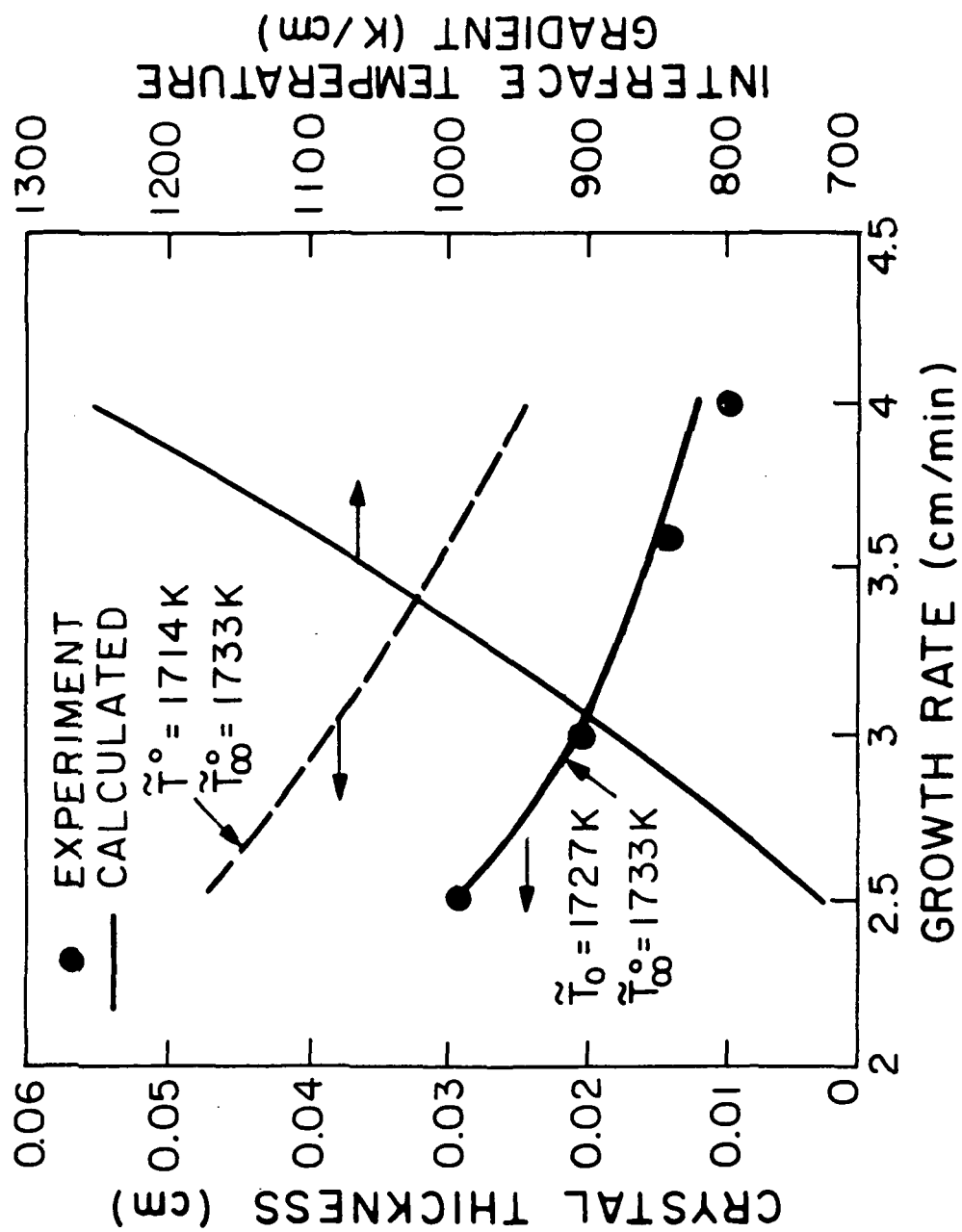
Fig. 2. Comparison of experimental and calculated t-V relationships for 10 cm wide ribbon.

6
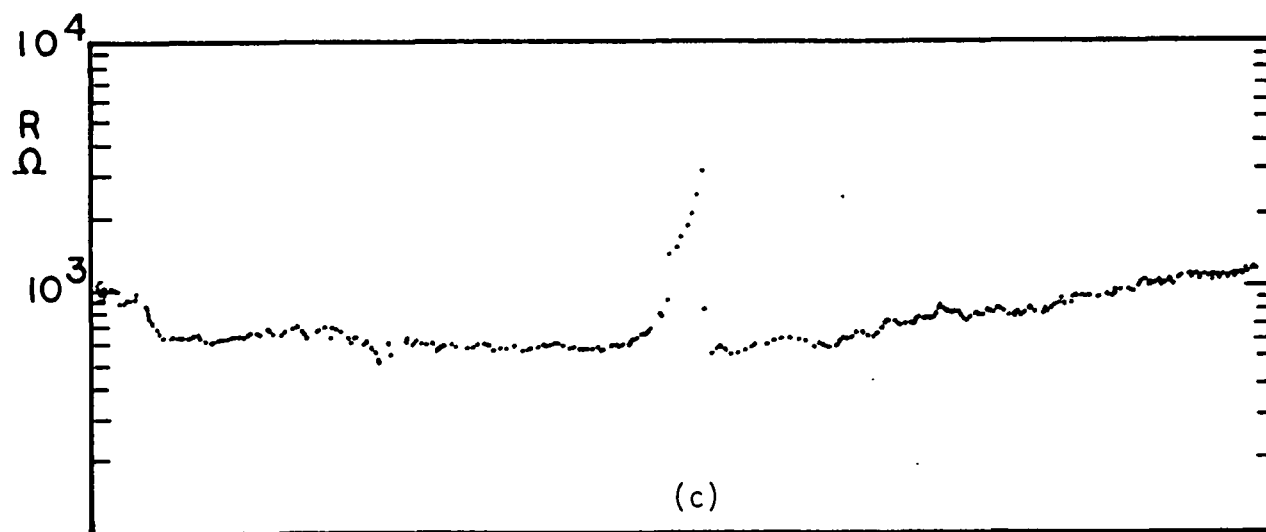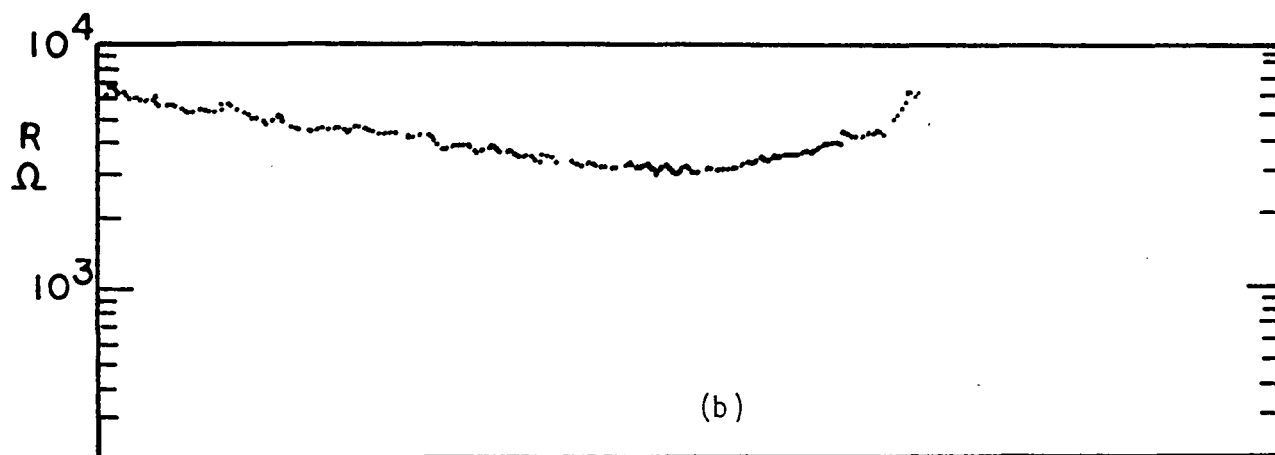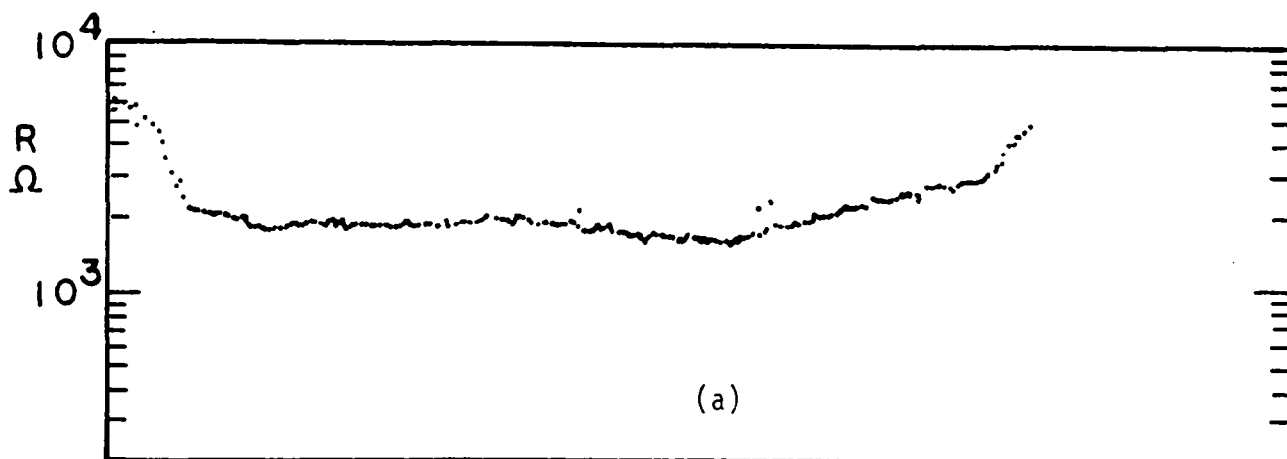
Fig. 3. Spreading resistance (resistivity) profiles for aluminum-doped
ribbon grown at 2.5 cm/min. Traces (a), (b), and (c) are for the
ribbon represented in curves (a), (b), (c) in Fig. 1a. The traces
were taken down a $2°52'$ level through the ribbon thickness.

(a) Melt/solid interface shape

(b) 2.5 cm/min

(c) 3.0 cm/min

(d) 3.5 cm/min

(e) 4.0 cm/min
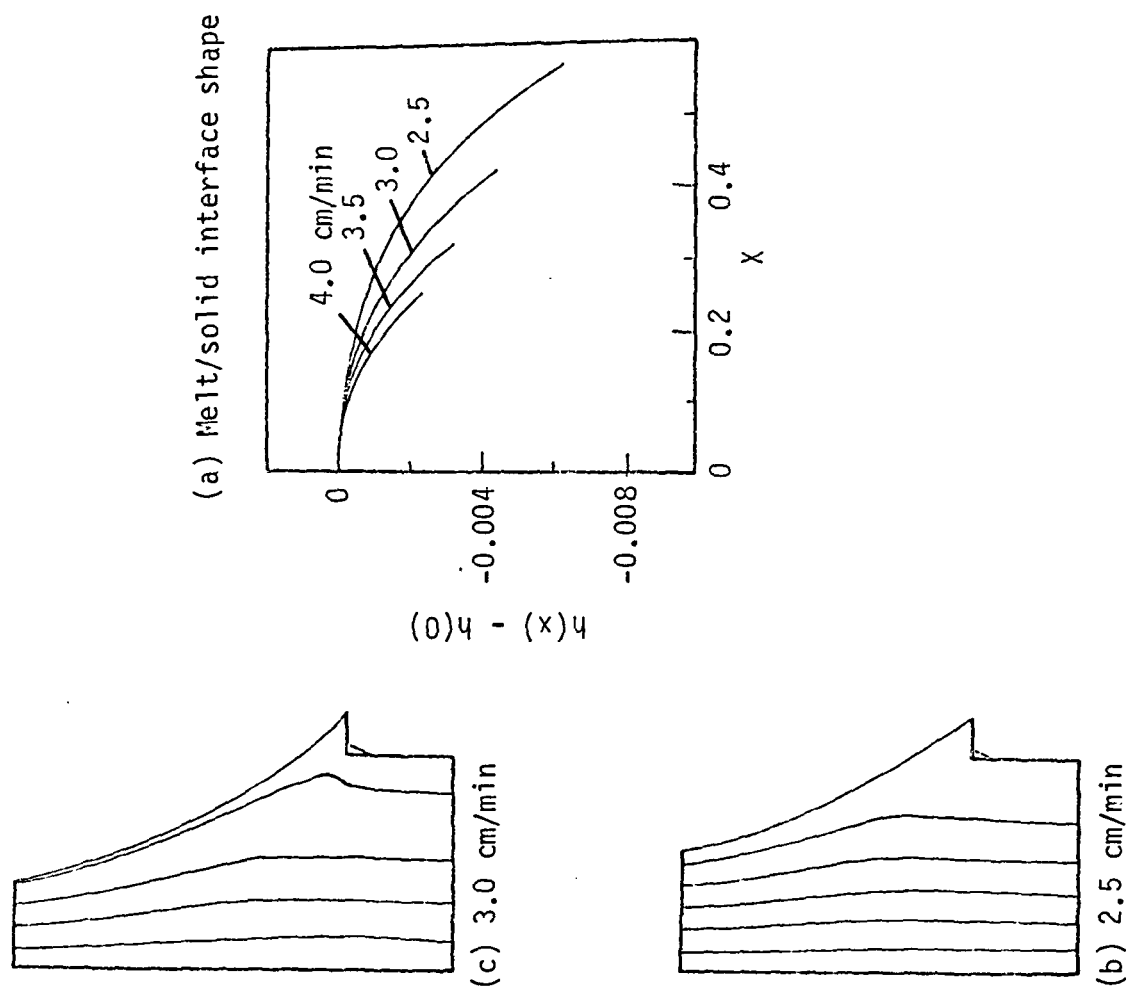
Fig. 4.   Interface shapes (a) and associated die top and meniscus melt streamlines (b)-(e) calculated for ribbon growth in system represented in Fig. 2.

solute concentration that is higher at the centerline than at the crystal surface. Figures 4b, 4c, 4d, and 4e show the calculated streamlines at growth rates of 2.5, 3, 3.5, and 4 cm/minute. In all cases, a converging flow field develops. As a result, higher solute concentration is also obtained at the centerline, because of lateral convection.

The isoconcentration lines and the interface concentration displayed in Figure 5 are calculated for a solute with equilibrium distribution coefficient of 0.1 and a diffusion coefficient equal to that of aluminum (0.0005 cm^2/s) [4]. As shown in Figures 5b, 5c, 5d, and 5e, the isoconcentration lines for the interfaces in Figure 5a become more squeezed into the melt/solid interface as the growth rate is increased. Regardless of the increase in the growth rate, magnitude of the dopant segregation along the interface is decreased from 10.56, 9.27, 7.84 to 6.64 at growth rates of 2.5, 3, 3.5, and 4 cm/minute, respectively. This behavior is caused by the continuous decrease in the net deflection of the melt/solid interface as the growth rate is increased. Further decreases in the magnitude of the equilibrium distribution coefficient results in a very small change in the segregation magnitude; e.g., at a growth rate of 2.5 cm/minute dopant segregation is equal to 10.56, 11.29, and 11.54 for K_o of 0.1, 0.05, and 0.01, respectively.

These results suggest that for aluminum, K_o = 0.002; segregation as predicted by the finite element model will remain within the range measured experimentally.

The success of the initial fitting between the predictions of the finite element model and the experimental measurements suggest further application of the model is useful to simulate and study other EFG configurations and also to continue analysis of the available experimental data. In the next step, the Marangoni convection will be invoked in both of the thermal and mass transfer models. The results of this step should confirm the absence of Marangoni convection in the experiment, since very large solute segregations are expected to occur because of the high intensity of the flow field. These calculations will be followed by investigation of the system stability caused by thermocapillary effects, where at high growth rates and static heads the meniscus becomes unstable and as a result the crystal pulls free. This behavior has been modeled and studied for a prototype EFG configuration (using the same system parameters of reference [1]), where Newton's method and the continuation technique were employed to calculate the critical points of stability.

2. <u>Stress Analysis</u> (J.C. Lambropoulos and J.W. Hutchinson, Harvard University)

The calculations of stress distributions with high rates of plastic deformation were reported in the last quarterly [5] to be only approximately correct. More detailed investigation into the numerical schemes that are used in the analysis has been carried out to check various aspects of the calculation. The cause of the difficulties in obtaining physically meaningful solutions has been traced to an inadequacy of the grid size very close to the growth interface to handle the very large changes in stress and strain rate that are imposed for the high creep intensity predicted by the data of Siethoff and Schröter [6].

9

(a) Melt/solid interface concentration
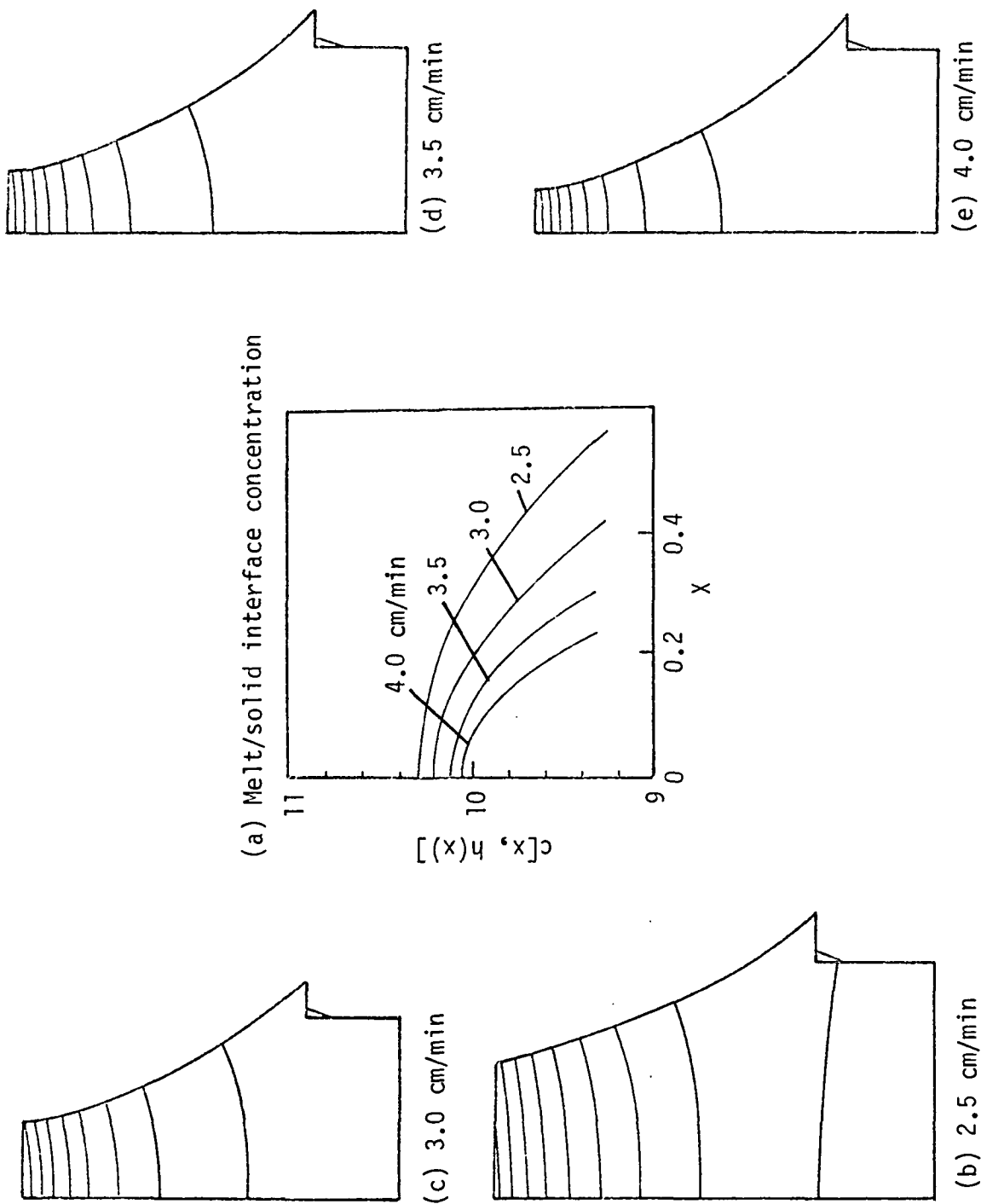
(b) 2.5 cm/min

(c) 3.0 cm/min

(d) 3.5 cm/min

(e) 4.0 cm/min

Fig. 5. Interface shapes (a) and associated isoconcentration lines (b)-(e) for an impurity with $K_0 = 0.1$ and $D = 5 \times 10^{-4}$ cm^2/s calculated for ribbon growth in system represented in Fig. 2.

The difficulty in dealing with the high rate of change of the variables near the growth interface appears to also occur in modeling of non-zero interface stresses. Rather than attempt to increase grid size to deal with this problem, investigation of a simpler scheme to study the high strain rate cases has been initiated. It appears that a physically valid approximation in this situation is to assume that $\dot{\varepsilon}_{yy}$, the transverse shear strain rate, is essentially zero very close to the growth interface. This leads to some simple relations between the creep and thermoelastic strain rate components acting on the sheet. It is also evident that in this limit, the use of a zero interface stress component σ_{yy} boundary condition is justified. Essentially, the calculation results then become independent of σ_{yy}.

Details of this new approximation to account for high interface stresses will be reported in the future.

B. Creep Law Studies

Creep response of silicon has been studied in four-point bending of both CZ silicon and of ribbon at temperatures above 1000°C. The results on the defect structure are reported below.

1. CZ Silicon

CZ silicon wafers with (100) surface orientations were subjected to incremental loading at 1215°C and at 1360°C. The loads were chosen to arrive at comparable total strains of the order of 1×10^{-4}.

The loading conditions were described in the previous quarterly report [5]. The stress acting on the samples was calculated assuming that a linear stress distribution exists across the thickness of the samples, as shown in Fig. 6. Loads were applied by increasing the force on the sample with four-point bending until maximum sample surface stresses were of the order of 10 MPa. After a final displacement of the order of 0.1 cm was obtained, the load was removed and the samples cooled to room temperature.

Cross-sectional micrographs of the CZ samples have been made along a longitudinal plane perpendicular to the bending axis, as illustrated in Fig. 6. The dislocation structures observed at locations of the samples marked A, B, and C in Fig. 6 are given in Figs. 7 and 8 for the 1215°C and 1360°C experiments, respectively.

At 1215°C, the unstressed region A of the sample remains dislocation free (Fig. 7(a)). The high density of etch pits appears to be related to B-swirl defects found often in as-grown CZ silicon. This contrasts to the results at 1360°C, where a dislocation density in excess of $1 \times 10^5/cm^2$ is produced. It is possible that these dislocations have migrated into the stress-free region, given the long time (3.5 hours) during which the sample was under stress. A second source of dislocations is from point defect condensation, whereby the B-swirls are assumed to coalesce into A-swirls of dislocation loop-type defects.
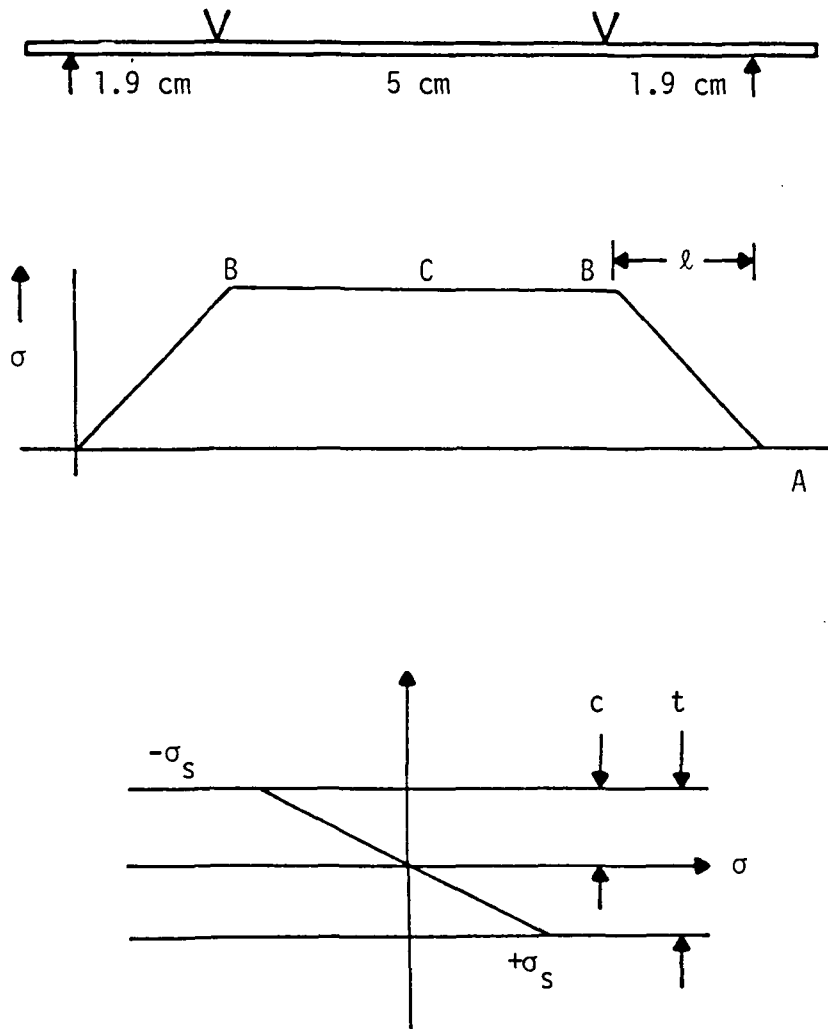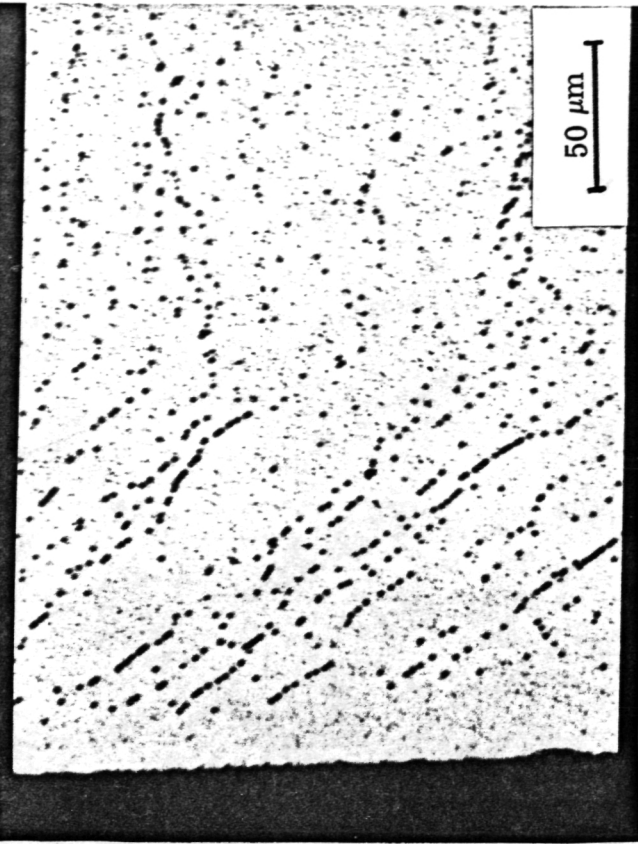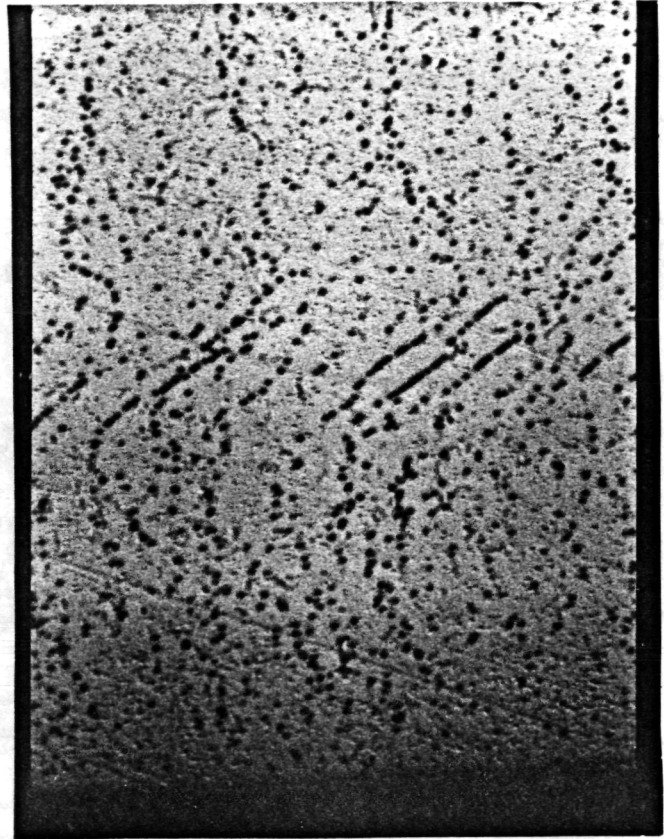
11

Fig. 6. Schematic of stress distribution.
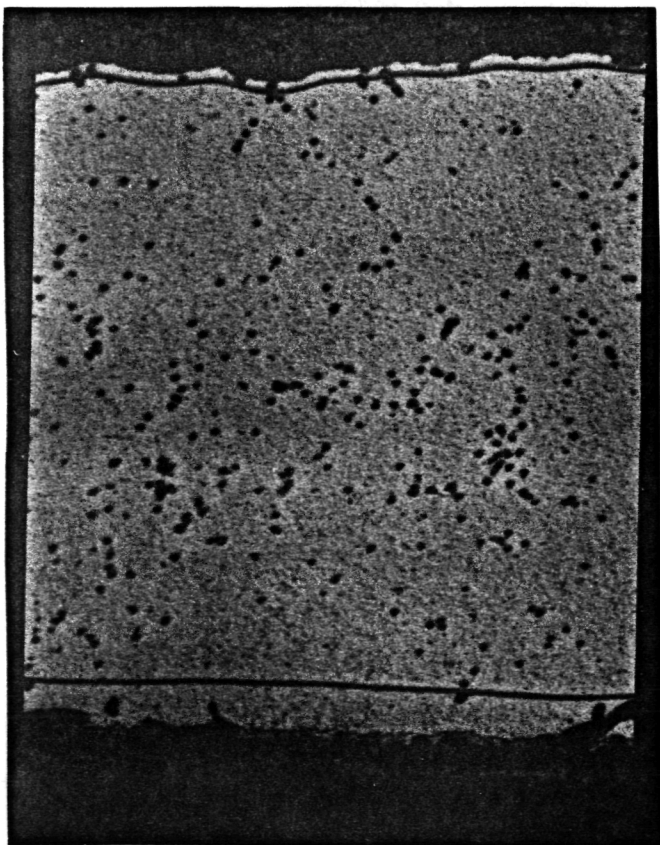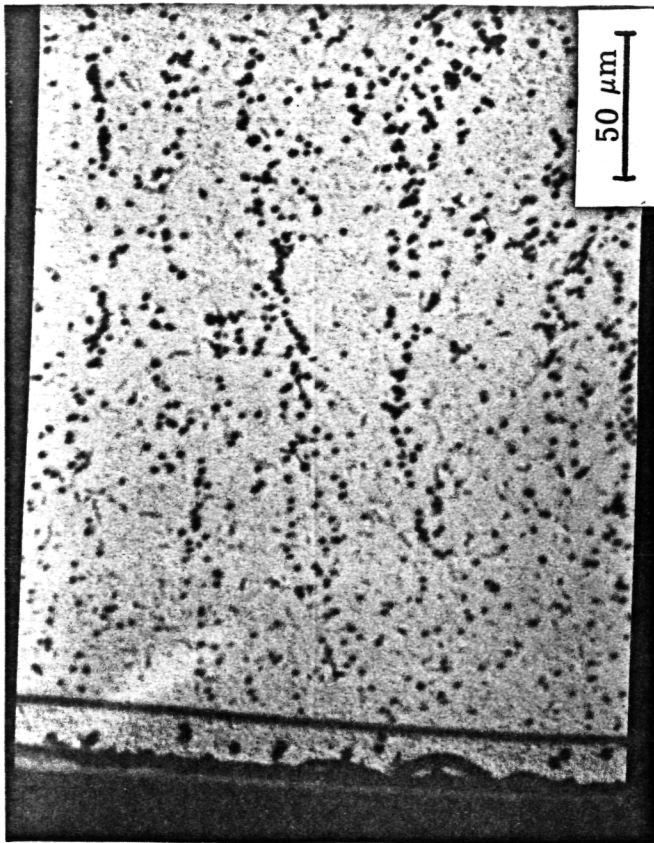
Region A, $N_D = 0$.

Region B, $N_D = 1.0E6/cm^2$.
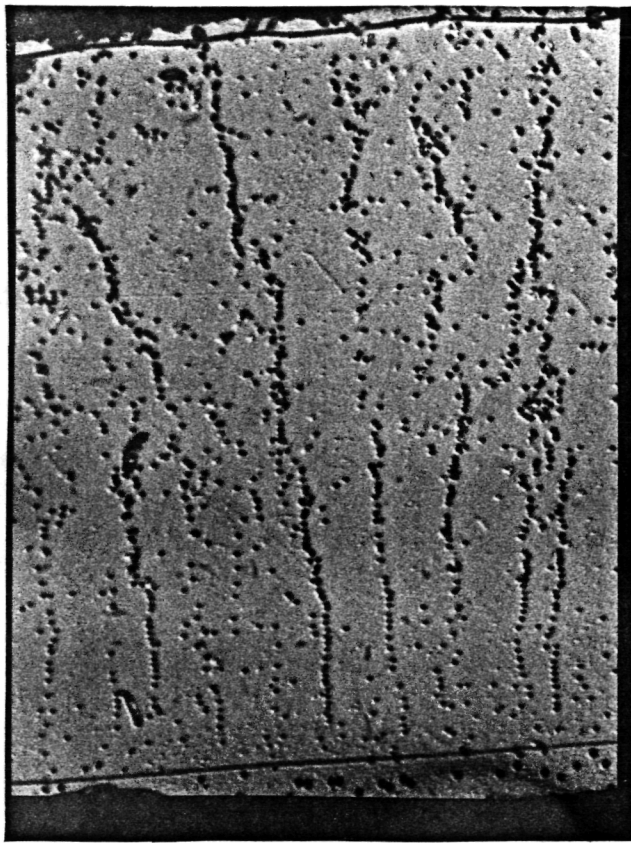
Region C, $N_D = 1.4E6/cm^2$.

Fig. 7. (100) Czochralski silicon stressed at 1215°C.

Region B, N_D = 1.6E6/cm^2.

Region A, N_D = 4.3E5/cm^2.

Region C, N_D = 1.8E6/cm^2.

Fig. 8. (100) Czochralski silicon stressed at 1360°C.

In the transition region B of intermediate stresses, samples at both temperatures show dislocation densities of $1 \times 10^6/cm^2$ and above (Figs. 7(b) and 8(b)). In addition, spatial nonuniformities occur, possibly due to the onset of polygonization.

In the region C of highest and most uniform stress, dislocation densities are at $1.4 \times 10^6/cm^2$ and $1.8 \times 10^6/cm^2$ for the $1215^\circ C$ and $1360^\circ C$ samples, respectively. Again, distinct banding that leads to nonuniform dislocation distributions is observed.

Some differences in the distributions through the thickness are observed at the two temperatures. This may be due to orientational effects as no effort was made to orient the samples with respect to the bending axis in these initial experiments. Future experiments with oriented wafers are planned.

2. Ribbon

Ribbon was stressed in the four-point bending apparatus at $1050^\circ C$. The purpose of these experiments was to examine the extent of the creep response that would arise under relatively short times of loading. The loading conditions and displacements are given in Table I. After the sample cooled, the remaining deflection was measured and compared to the deflection under load. The results given in Table I show that the creep in the loading time of 40 minutes is sufficient to make the strain permanent in most cases, and relatively little elastic spring-back occurs. Considerable variability in this data was observed in sample to sample, as is seen in the representative displacement-time graphs shown in Figs. 9(a) and 9(b) for some samples. This is attributed to inhomogeneities in the material itself as well as to geometric nonuniformities which result in nonreproducible loads. Applied stresses were in the range of 30-35 MPa for the light loads, and 80-90 MPa for the heavier ones.

It can be concluded from these experiments that creep can be still a very important factor in stress relaxation at temperatures of the order of $1000^\circ C$ during ribbon growth. The above results are for as-grown ribbon samples which have already undergone considerable work hardening in the _in situ_ furnace cool. Yet they still have a fast transient primary creep response under load. The data in Fig. 9 shows this is over in a time of the order of a minute or so. After steady-state creep sets in, it produces nearly complete relaxation in 20 minutes after application of the second load.

The samples were further cross-sectioned and the defect structure examined. It has been difficult to establish the nature of the dislocation structures caused by the additional creep in view of the already high dislocation density in the as-grown material. Additional work is being done to look at these samples in more detail.

3. Transient Creep Response

Emphasis here is on relatively short time ($\leq$ 10 minutes) non-steady-state behavior. Displacement time graphs have been generated for creep response of CZ and FZ silicon in order to compare the effect of impurities. The CZ wafer had measured substitutional carbon at 4.5×10^{17} at/cc and oxygen at

Table I. Four-Point Bending at 1050°C.

1. 40 minutes heat-up
2. 20 minutes under load L_1
3. 20 minutes under load L_2
4. Cool with no load

Sample No.	t (mm)	L_1 (g)	d_1 (mm)	L_2 (g)	d_2 (mm)	Final d (mm)
1	0.45	163	0.10	453	0.28	0.23
2	0.36	163	0.20	435	0.76	0.64
3	0.25	81	0.09	214	0.74	0.74
4	0.25	81	0.09	214	0.76	0.48
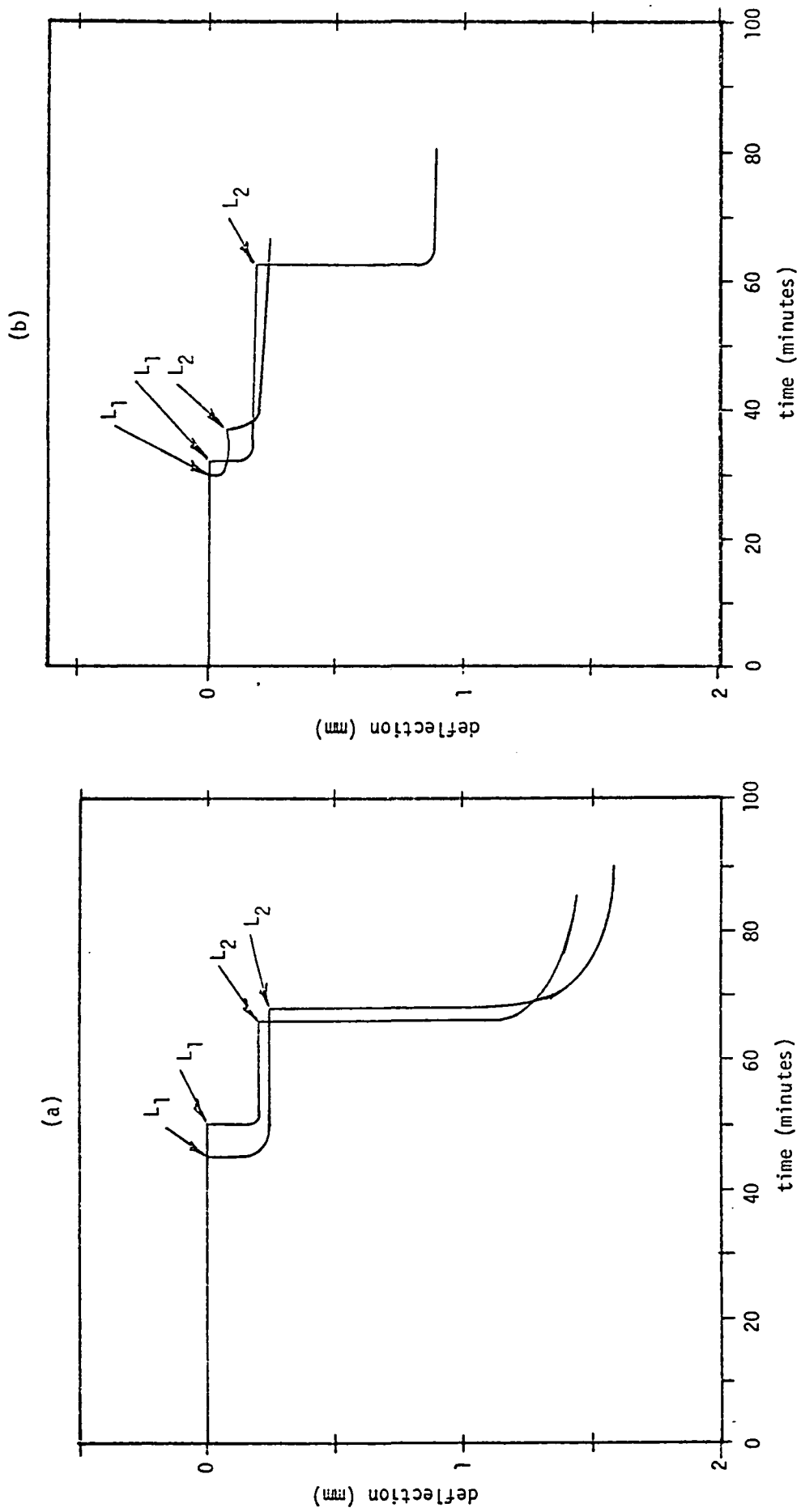
Fig. 9. Response of ribbon stressed in four-point bending at $1050^{\circ}C$ under loads of $L_1 = 170g$ and $L_2 = 440g$.

17

1.0×10^{18} at/cc. The FZ wafer had nondetectable levels ($\leq 1 \times 10^{16}$ at/cc) for these impurities.

The displacement-time graphs generated at 1215°C for 10-second bending of the FZ (curve 1) and CZ (curve 2) and for 10 minutes for the CZ (curve 3) are shown in Fig. 10. It is evident that there is an order of magnitude difference in the strain rate between the FZ and CZ silicon, which can be attributed to impurities. The strain and strain rate data will be examined in relation to the defect distributions generated in these samples.

C. Fiber Optics Temperature Sensor

In the initial tests of the fiber optics based temperature sensor in the 10 cm cartridge, reliable and reproducible results were not obtained. Large variations in signal levels and differences from the calibration results obtained in a small test furnace occurred. The origin of the stray radiation was traced to the cartridge afterheater region, where the fibers passed very close to the active afterheater, rather than the probe tip. This was shown when the probe was rebuilt so that the tip was imbedded in the cold shoe and kept at temperatures below 300°C. Even then, the output signal was found to be dominated by variations in the afterheater temperature setting.

After these initial attempts to install the optical fiber sensor in the cartridge failed, it was decided to construct a new optical fiber probe. The entire optical fiber section will be enclosed in a water-cooled jacket, which will extend to within several mm of the probe tip. This probe will not have the flexibility of the initial one, which consisted essentially of the fibers themselves. An additional difficulty at this time arises because only short lengths of thick (1 mm) Al_2O_3 fibers are available, rather than the longer thinner (0.25 mm) ones desired. This requires use of quartz fibers and completes the construction and assembly of the entire probe. Some problems with alignment at the terminations of the Al_2O_3 and quartz have been experienced. We are still investigating the possibility of obtaining the longer Al_2O_3 fibers.

D. Residual Stress Measurements

A residual stress measurement technique using laser interferometry to measure sample deflection under load is being evaluated at the University of Illinois. The technique has been successfully applied to calculate applied in-plane stresses in CZ wafers. A description of the technique and results of this preliminary study are contained in Appendix III.

Modifications are under study to allow application of this method in the case of EFG ribbon. The main problem areas center around dealing with the irregular dimensions (surface striations and thickness nonuniformities) of the ribbon, which increases in complexity the fringe pattern generated, and in changes in fixturing and loading that are needed to accommodate the rectangular, rather than circular geometry.
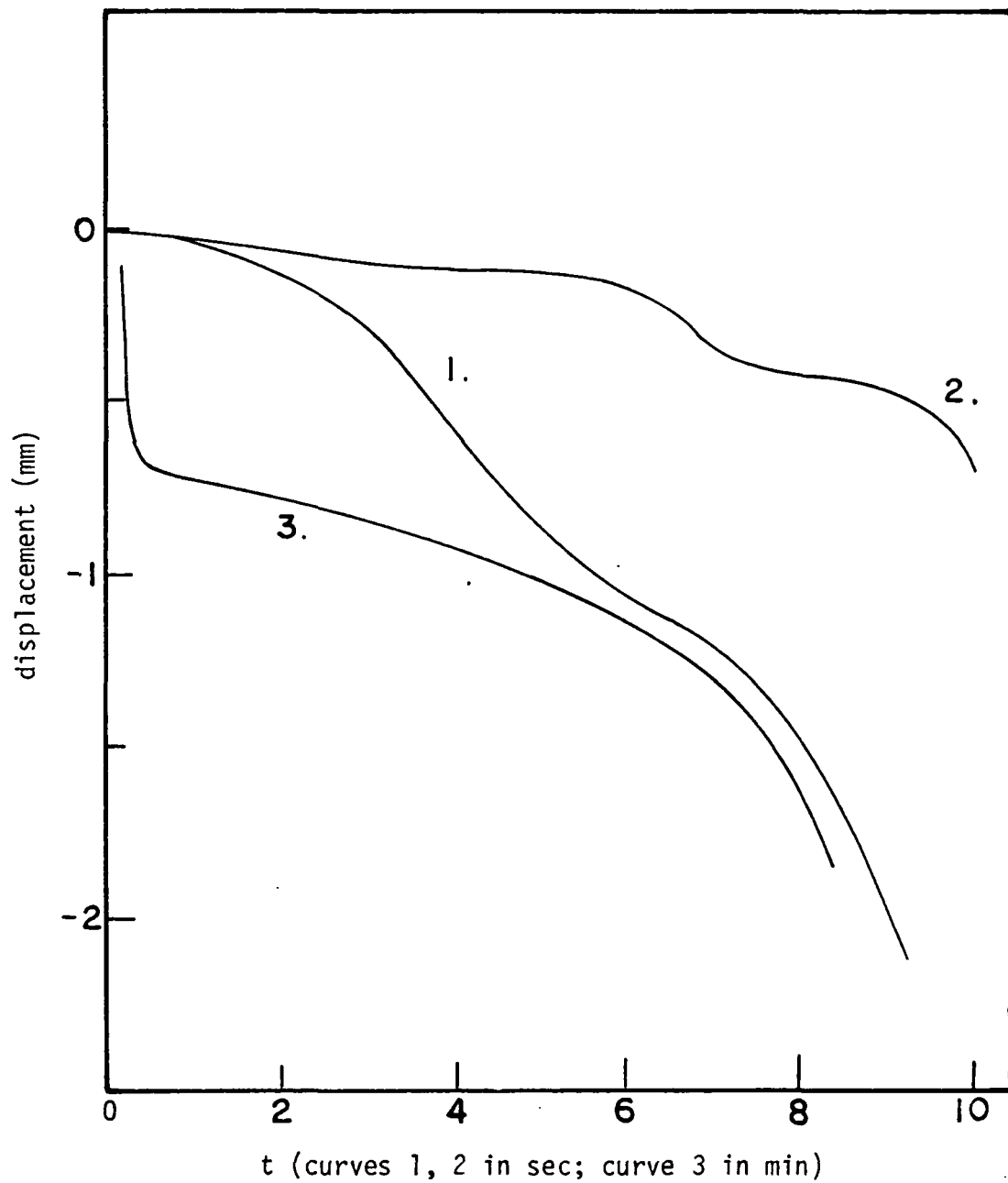
Fig. 10. Displacement-time graphs for four-point bending of FZ (curve 1) and CZ (curves 2 and 3) silicon wafers at 1215°C.

REFERENCES

[1] H.M. Ettouney, R.A. Brown, and J.P. Kalejs, Analysis of Operating Limits in Edge-Defined Film-Fed Crystal Growth, J. Crystal Growth, 62 (1983), 230-246.

[2] H.M. Ettouney and R.A. Brown, Mechanisms for Lateral Solute Segregation in Edge-Defined Film-Fed Crystal Growth, J. Applied Physics, in print, 1983.

[3] S.R. Coriell and R.F. Sekerka, J. Crystal Growth, 46 (1979), 479.

[4] J.P. Kalejs, G.M. Freedman and F.V. Wald, J. Crystal Growth, 48 (1980), 74.

[5] J.P. Kalejs et al., JPL 4th Quarterly Report, August 15, 1983.

[6] H. Siethoff and W. Schröter, Scripta Met., 17 (1983), 393.

Preceding Page Blank

APPENDIX I

WORK BREAKDOWN STRUCTURE AND PROGRAM PLAN

July 9, 1983 – July 8, 1984

"STRESS STUDIES IN EFG"

Subject	Description	JUL	AUG	SEP	OCT	NOV	DEC	JAN ('84)	FEB	MAR	APR	MAY	JUN	JUL
Theoretical	Modeling of reduced stress growth configurations.	X	-	-	-	-	-	-	-	-	-	-X		
Experimental	Advanced system design concept testing.				X	-	-	-	-	-	-	-X		
	High temperature creep measurements in silicon.	X	-	-	-	-	-X							
	Temperature measurements with optical fiber systems in support of modeling.	X	-	-	-	-	-X							
	Residual stress measurement technique development.	X	-	-	-	-	-X							
Program Management	Progress Reports, etc.	X	-	-	-	-	-	-	-	-	-	-X		

APPENDIX II

The following papers were presented at the Research Forum on High Speed Growth and Characterization of Crystals for Solar Cells, Port St. Lucie, Florida, July 25-27, 1983.

a. "The Effect of Creep on the Residual Stresses Generated During Silicon Sheet Growth", by J.W. Hutchinson and J.C. Lambropoulos, Harvard University.

b. "Mathematical Modeling of High-Speed Ribbon Systems: A Case Study of Edge-defined Film-fed Growth", by H.M. Ettouney and R.A. Brown, MIT.

c. "Experimental Aspects of the Study of Stress Generating Mechanisms in Silicon Sheet Growth", by J.P. Kalejs and R.O. Bell, Mobil Solar Energy Corporation.

They will appear in the proceedings of the Forum to be published by JPL.

Preceding Page Blank

APPENDIX III

Paper by A.T. Andonian and S. Danyluk on "Non-Destructive
Determination of Residual Stresses in Circular Silicon
Wafers", submitted for publication.

Preceding Page Blank

NON-DESTRUCTIVE DETERMINATION OF RESIDUAL STRESSES
IN CIRCULAR SILICON WAFERS

A. T. Andonian and S. Danyluk
Department of Civil Engineering, Mechanics and Metallurgy
University of Illinois at Chicago

Introduction

In many instances, a predominant factor contributing to the failure of structural components is the magnitude of residual stresses. Generally, restraint limits the distortion but in some instances large local strains can arise which increase the risk of failure. Residual stresses can also contribute to fatigue failure, brittle fracture, structural instability, stress corrosion and in some cases cause premature buckling and warping or result in a dramatic reduction in the components resistance to brittle fracture.

Manufacturing and fabricating processes are the most common causes of residual stress. Processes such as casting, welding, cutting, machining, molding and heat treatment introduce residual stresses [1-6]. For example, residual stresses can arise from thermal gradients in the components in processing and the unavoidable restraint offered by the surrounding structure. In addition, stresses can be generated during metal shrinkage. These stresses can be minimized to some extent by a careful control of the cooling rate, material chemistry or transformation characteristics, and both the internal and external restrain conditions.

Residual stresses are particularly important in non-metallic plates such as semiconductor or ceramic sheet materials because the geometries are particularly conducive to buckling which in some cases can lead to fracture. For example, in the semiconductor industry, silicon is produced in thin sheet for the manufacture of large scale integrated circuits and solar arrays. In these cases growth conditions may influence precipitate (oxide) formation which leads to buckling of the ribbon in addition to influencing the electrical properties.

Measurement of Residual Stresses

Measurement of residual stress cannot be accomplished by the conventional non-destructive methods of experimental stress analysis. The strain sensor (strain gage, photoelastic coating, Moire grating, etc.) being totally insensitive to the loading history of the component, measures only changes in strain after installation of the sensor.

There are several non-destructive techniques available for determining residual stresses [7-13]. The two most widely used are the 'X-ray diffraction technique' and the 'blind-hole drilling' method. Both techniques have limited applicability depending on the material and component size. Aside from the bulk and complexity of the equipment, the X-ray technique is limited by the X-ray absorption which occurs within several micrometers of the surface depths and limits the measurement of residual stress to these depths. The resolution of this technique is approximately 30 MPa for steel over several mm^2 in area. In the blind-hole drilling method a special rosette strain gage is bonded to the test specimen. A small hole (typically 1.5 to 3 mm in both diameter and depth) is then drilled through the center of the gage and the resulting change in strain around the hole due to relaxation is measured. Residual stresses are obtained from the strains by analytic methods. Blind-hole drilling is a semi-destructive technique and it measures the average strain within the top surface layers at a very specific location. This technique is limited to thick samples and cannot be used for thin silicon plates since the drilling procedure can noticeably impair the structural integrity of the part being tested.

Both techniques are unsatisfactory for measuring residual stresses because only stresses within the top few millimeters at specific locations are measured and full field, through the tickness residual stresses are usually desired. Moreover, considering the additional limitations imposed by thin plates it can be concluded that these requirements can present formidable obstacles in determining residual stresses.

In this paper, a laser interferometry technique [14,15] for measuring deflections over large spatial dimensions is described. These measurements, when combined with an analysis for predicting deflections in linear-elastic plates, lead to the residual stresses. This paper outlines the procedure for obtaining the residual stresses from the experimental measurements in thin circular plates.

Description of the Technique

The technique largely depends on the ability to measure deflections of thin plates when the applied loads are known. Figure 1 shows a schematic of the supporting and loading geometry. A circular thin plate is simply supported along the edge end loaded at the center. The true deflections can be measured by laser interferometry; the experimental arrangement of which is shown in Fig. 2. The coherent light produced by a helium-neon laser is diverged and collimated by an optical system. The uniformly expanded beam (10 cm in diameter) emerging from the parabolic mirror is reflected onto the specimen by a broadband beamsplitter inclined at 45° to the optical axis. The return beam from the polished surface of the specimen is converged by a convex lens after

passing through the optical flat and the beamsplitter. Finally, the converged light beam carrying the optical information (interference pattern) is recorded by a camera.

The constructive and destructive interference of the monochromatic light source occurs in the following way. The monochromatic light is directed perpendicular to the specimen and reflected from the bottom surface of the optical flat and the top surface of the specimen and viewed in reflection. Destructive interference (dark fringes) occurs when the optical path difference (2ρ) is an odd number of half wavelengths $\lambda/2$

$$2\rho = \left(n - \frac{1}{2}\right)\lambda \qquad n = 1,2,3,\ldots \tag{1}$$

Constructive interference (light fringes) occurs when

$$2\rho = n\lambda \qquad n = 1,2,3,\ldots$$

The interference pattern can be analyzed to yield full-field plate deflection to an accuracy of half wavelength.

Determination of Residual Stresses from Deflections

Consider a plate element such as shown in Fig. 3. Taking the sum of the projections in the radial direction of the in-plane forces acting on the element, we obtain

$$N_r - N_t + \frac{dN_r}{dr} = 0 \tag{2}$$

where $N_r = \sigma_r h$ and $N_t = \sigma_t h$ are the radial and tangential components of the stress residuals, σ_r and σ_t the average residual stresses and h

the plate thickness. Also, as given in reference [16] the governing
plate equation can be expressed in the following form

$$D\left(\frac{d^3\omega}{dr^3} + \frac{1}{r}\frac{d^2\omega}{dr^2} - \frac{1}{r^2}\frac{d\omega}{dr}\right) = N_r\frac{d\omega}{dr} + \frac{p}{2\pi r} \quad . \tag{3}$$

where

$$D = \frac{Eh^3}{12(1-\mu^2)}$$

E = Young's modulus

μ = Poisson's ratio

w = deflection

r = radial distance measured from point of loading

Solving for N_r we get

$$N_r = \left(\frac{d\omega}{dr}\right)^{-1}\left[D\left(\frac{d^3\omega}{dr^3} + \frac{1}{r}\frac{d^2\omega}{dr^2} - \frac{1}{r^2}\frac{d\omega}{dr}\right) - \frac{p}{2\pi r}\right] \tag{4}$$

Hence the residual stresses may be obtained if the deflection is known
as a function of r.

The experimentally determined deflection ω_{exp} obtained from the
interference pattern may be represented in the simplest functional form
as a third degree polynomial

$$\omega = Ar^3 + Br^2 + Cr + F$$

in the vicinity of any point Q (see Fig. 4). The constants A, B, C
and F may be found given ω_i at r_i (i = 1,2,3,4) as

$$
\begin{bmatrix} \omega_1 \\ \omega_2 \\ \omega_3 \\ \omega_4 \end{bmatrix} = \begin{bmatrix} r_1^3 & r_1^2 & r_1 & 1 \\ r_2^3 & r_2^2 & r_2 & 1 \\ r_3^3 & r_3^2 & r_3 & 1 \\ r_4^3 & r_4^2 & r_4 & 1 \end{bmatrix} \begin{bmatrix} A \\ B \\ C \\ F \end{bmatrix}
\tag{5}
$$

Once A, B, C and F are found the derivatives of the experimenal deflection curve at point Q can be evaluated as

$$
\frac{d\omega}{dr}\bigg|_Q = 3Ar_Q^2 + 2Br_Q + C
\tag{6}
$$

$$
\frac{d^2\omega}{dr^2}\bigg|_Q = 6Ar_Q + 2B
$$

$$
\frac{d^3\omega}{dr^3}\bigg|_Q = 6A
$$

Equations (6) can be substituted into Eq. (4) to give the experimental N_r at point Q as

$$
N_r = \frac{D\left(9A - \dfrac{C}{r_Q^2}\right) - \dfrac{P}{2\pi r_Q}}{3Ar_Q^2 + 2Br_Q + C}
\tag{7}
$$

This procedure can be repeated (n-3) times if there are n experimental data points. The values of N_r can then be plotted versus r. After plotting the experimental values of N_r along a radial line, Eq. (2) can be used in conjunction with this plot to give the experimental N_t distribution.

Experiments

The technique described above was used to determine residual stresses in a single crystal, 0.575 mm thick and 6.25 cm in diameter Czochralski silicon wafer. The optical system presented in Fig. 2 and a fixture capable of testing circular wafers under axisymmetric loading were built. The specimen was simply supported with a supporting edge diameter of 89 mm (2a). The interference pattern before loading and under the applied load was recorded with a 4 x 5 camera. A typical interference pattern for the silicon wafer is shown in Fig. 5. Each fringe spacing represents an incremental deflection of 315 nm which is half the wavelength of the He-Ne laser. A nikon comparator (6C-2) was used to determine the fringe locations with high accuracy. Values of fringe order and corresponding centroidal distances were recorded to generate surface profiles along eight radial lines. Local deflections were found and fed into a computer program to evaluate stress residuals along these lines according to the analysis described in the previous section.

Results and Discussion

A data set including fringe orders, radial distances, deflections and residual stress values are presented in Table I. The radial distances were measured from the point of load application. The central deflection of the plate, w_{max}, was measured independently. The fringe orders were numbered such that the first contour around the point of loading was of zero order. The deflections were then found as:

$$w_Q = w_{max} - n_Q \frac{\lambda}{2}$$ (8)

where

w_Q = deflection at point Q

η_Q = fringe order at point Q

λ = wavelength (628 nm)

The combined resolution of the optical setup and the comparator in determining the fringe locations was 1 μm.

A topographic scheme was used to plot the constant value contour line systems for the average residual stress $\overline{\sigma_r}$ which is shown in Fig. 6. Only the central region of the circular wafer was analyzed which represents an area of 28 cm^2. The sensitivity of this integrated technique in determining residual stresses is found to vary between 100KPa and 500KPa. Applied flexural load, plate curvature, fringe density and optical alignment can be listed among the parameters effecting the uncertainty. A detailed sensitivity analysis for different plate geometries will be the subject of a subsequent paper.

Acknowledgement

REFERENCES

[1]   W. M. Baldwin, Jr., Proc. ASTM, 49, 1 (1949)

[2]   D. G. Richards, Residual Stress   Measurements, p. 210.
       ASM Publ. (1952).

[3]   E. G. Signes, Brit. Weld. J., 14, 108 (1967).

[4]   C. L. Formby and J. R. Griffiths, Proc. Weld. Inst. Conf. p.359.
       (1977).

[5]   G. A. Alpsten and L. Tall, Welding J., 49, 93 (1970).

[6]   I. Tatsukawa and J. Ida, Trans. Jap. Weld. Soc., 3, 275 (1973).

[7]   J. T. Norton, Materials Evaluation, 31, 21 (1973)

[8]   M. James and J. B. Cohen, ASTM J. of Testing and Evaluation, 6, 91
       (1978).

[9]   R. G. Bathgate, Strain J. of BSSM 4, 20 (1968).

[10]   H. Fukuoka, H. Toda and H. Naka, Exp. Mech., 23 120 (1983).

[11]   V. Wilhelmy and H. Kubler, Proc. of SESA, 30, 142 (1973).

[12]   J. H. Underwood, Proc. of SESA, 30, 373 (1973).

[13]   N. Tebedge, G. Alpsten and L. Tall, Proc. of SESA, 30, 88 (1973).

[14]   A. S. Kobayashi, Exp. Tech. in Fracture Mech., II, p 59, ISU Press
       and SESA Publ., Conn. (1975).

[15]   J. H. Underwood, H. L. Swedlow and D. P. Kendall, Eng. Fracture
       Mech. 2,183 (1971).

[16]   S. P. Timoshenko and S. Woinowsky − Kreiger, Theory of Plates and
       Shlls, McGraw Hill (1959).

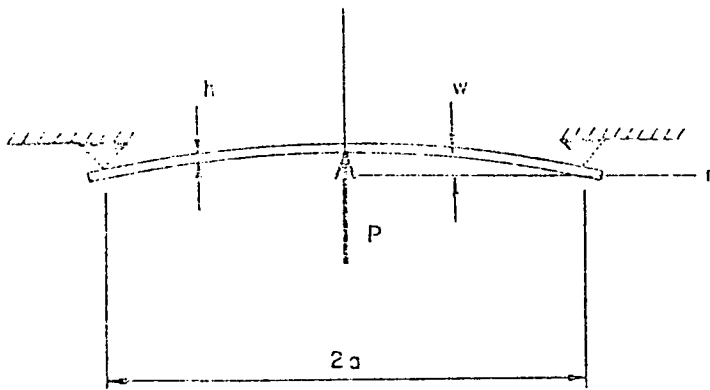Abbreviated Paper − For further information please contact the authors.

Fig. 1
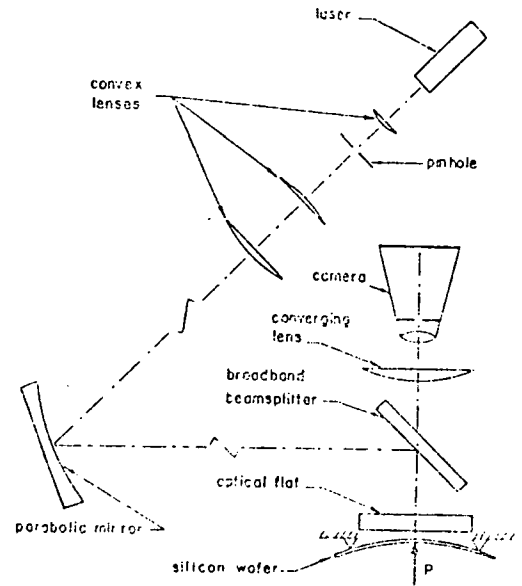Simply supported circular wafer
under centric loading

Fig. 2
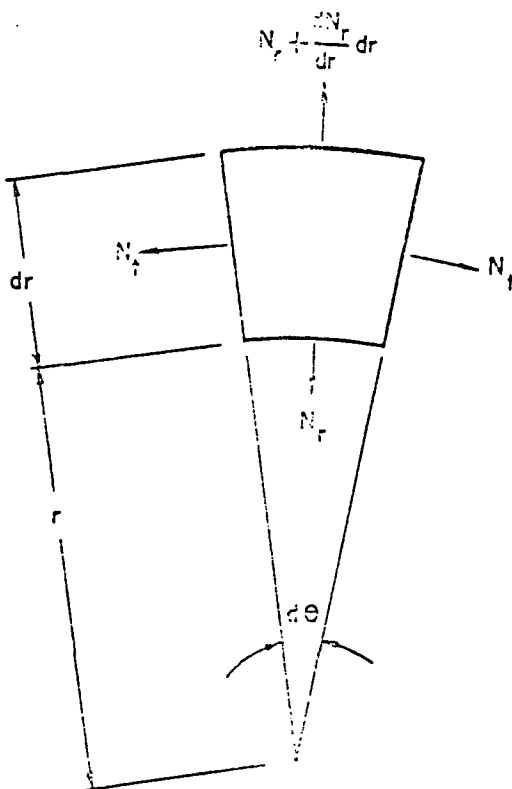Schematic of the experimental setup

Fig. 3
Definition of the stress
residuals on a plate element
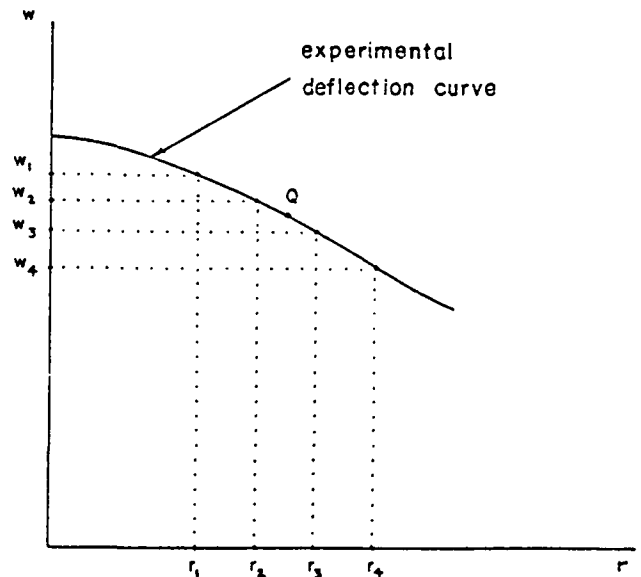in polar coordinates

Fig. 4
Presentation of data points around
point Q where residual stresses
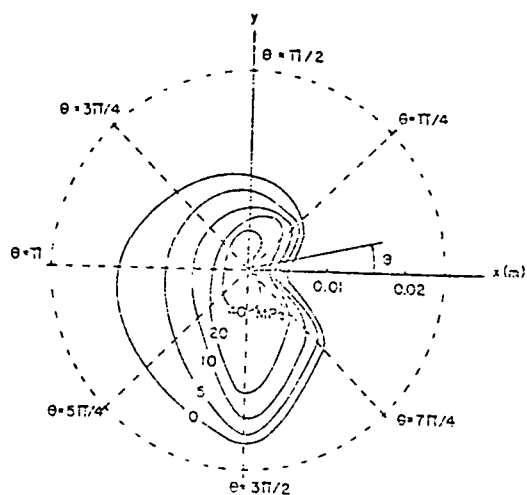are evaluated

Fig. 5

Typical interference pattern

Fig. 6

Distribution of the average residual stress $\overline{\sigma}_r$

TABLE I Typical Data Set			
Fringe Order	Radial Distance	Deflection w (m)	Avg. Residual Stress $\overline{\sigma}_r$
5	0.009674	0.000051322	
6	0.009983	0.000051008	5.5 MPa
7	0.010287	0.000050694	
8	0.010587	0.000050380	(at $r_Q = 0.01$m)
37	0.014641	0.000045670	
38	0.014890	0.000045356	-2.66 MPa
39	0.015136	0.000045042	
40	0.015377	0.0000447 28	(at $r_Q = 0.015$m)